

Capillary waves at the liquid-vapor interface and the surface tension of water models

Ahmed E. Ismail, Gary S. Grest, and Mark J. Stevens
Sandia National Laboratories, Albuquerque, NM 87185
 (Dated: May 25, 2019)

Capillary waves occurring at the liquid-vapor interface of water are studied using molecular dynamics simulations. In addition, the surface tension, determined thermodynamically from the difference in the normal and tangential pressure at the liquid-vapor interface, is compared for a number of standard three- and four-point water models. We study four three-point models (SPC/E, TIP3P, TIP3P-CHARMM, and TIP3P-Ew) and two four-point models (TIP4P and TIP4P-Ew). All of the models examined underestimate the surface tension; the TIP4P-Ew model comes closest to reproducing the experimental data. The surface tension can also be determined from the amplitude of capillary waves at the liquid-vapor interface by varying the surface area of the interface. The surface tensions determined from the amplitude of the logarithmic divergence of the capillary interfacial width and from the traditional thermodynamic method agree only if the density profile is fitted to an error function instead of a hyperbolic tangent function.

I. INTRODUCTION

The ability to derive accurate property predictions for the liquid-vapor interface is a key test for an atomistic force field. Because of the frequent occurrence of water in systems of chemical and biological interest, interfacial property prediction is especially vital for force fields of water. The most important of these properties is surface tension, an intensive quantity that measures the differential surface work required to increase the interfacial area. Accurate models of the surface tension of water are essential for conducting large-scale simulations of the wetting and spreading of water droplets at surfaces.

An interface between two distinct thermodynamic phases can be characterized by a local gradient of an order parameter whose mean value changes between phases, such as the boundary between a liquid and its own vapor below the critical temperature T_c . For simple fluids, thermodynamic arguments predict that the interfacial width Δ depends only on temperature and the interaction energies within each phase and across the interface. However, the presence of the interface breaks the translational invariance of the system, inducing Goldstone fluctuations or “capillary waves” at the interface [1, 2]. Density functional studies suggest that the surface tension predicted by capillary-wave theory exhibits a minimum as a function of the wavelength [3]. Previous studies of capillary waves involving water have tended to focus on liquid-liquid interfaces or on model fluids [4, 5], and have generally examined relatively small systems of less than 10,000 molecules; the present study represents the first study of capillary-wave behavior at the liquid-vapor interface of water.

For two-dimensional interfaces, these noncritical fluctuations give rise to a logarithmic increase in the interfacial width Δ with increasing L_{\parallel} , the length of the interface. Most previous simulations [6, 7] of the liquid-vapor interface in three dimensions did not investigate the dependence of Δ on the size of the interface. The purpose of this paper is to present atomistic molecular dynamics (MD) simulations of the liquid-vapor interface

of water. In particular, we obtain the surface tension γ in two different ways: from the difference in pressure parallel p_{\parallel} and perpendicular p_{\perp} to the interface (γ_p), and from the dependence of Δ on L_{\parallel} (γ_w). We confirm the previous result that γ_w depends on the functional form chosen to fit the order parameter (density profile) through the interface [8]. In particular, fitting the order parameter to an error function gives results for γ_w which are in strong agreement with γ_p . However, fitting our data to a hyperbolic tangent function, a functional form derived from mean-field arguments [2], gives results for γ_w which are systematically smaller than γ_p and further away from experimental results.

There are currently a large number of different atomic models for water. Guillot provides an extensive list of models developed through 2001 [9]; several additional models have been introduced since then [10, 11, 12, 13]. The simplest of the commonly-used atomic models, the SPC model [14], is a rigid three-point model with fixed charges; the most complex model, the POL5 model [15], is a polarizable five-point model. Most of the commonly used models are three- and four-point models. In three-point models, such as SPC/E [16] and TIP3P [17], the electric charges are assigned directly to the hydrogen and oxygen atoms; four-point models, such as the TIP4P [17] and Watanabe-Klein [18] models, locate the negative charge at a massless point a fixed distance away from the oxygen atom. Five-point models, such as TIP5P [19], and the early Bernal-Fowler [20] and ST2 [21] models, represent the negative charge of the oxygen using a pair of massless charges to capture the quadrupolar behavior of water. Polarizable models, including the SPC/FQ and TIP4P/FQ models [22], allow the magnitude of the point charges to be treated as variables which can fluctuate according to the local environment.

The proliferation of models has been motivated largely by the need to reproduce various physical and thermodynamic properties, such as the bulk density, the oxygen-oxygen radial distribution function, the heat of vaporization, and the diffusion coefficient. However, some models, such as the recent TIP3P-Ew [11] and TIP4P-Ew models

[12], are reparameterizations of existing models designed to account for changes in the treatment of long-ranged electrostatic interactions.

Most of the available water models adequately represent at least some of the thermodynamic properties of water; for a comprehensive review, see Jorgensen *et al.* [13]. Kuo *et al.* have shown that the changes introduced between, for example, the TIP4P and TIP4P/FQ models have little influence on properties such as the bulk liquid density or the mean distance between oxygen atoms either in bulk or at the interface [23]. However, the simulation behavior of models with nearly identical parameters can be markedly different: Mark and Nilsson have noted significant variation in physical and thermodynamic properties such as the self-diffusion constant and the radial distribution function of various three-point water models [24, 25]. Less is known about how well the various water models describe the liquid-vapor interface and the surface tension γ . Our own work, however, suggests that even models with very similar density and distribution profiles can have quite different predictions for surface tension.

Experimental studies demonstrate that the surface tension of water decreases with a slight quadratic dependence on temperature in the range $273\text{ K} < T < 373\text{ K}$ [26, 27, 28, 29, 30]. Surface tension results for higher temperatures have not been reported in the literature; we extrapolate the reported experimental data to higher temperatures. There have been a few studies for various three-point models [10, 31, 32, 33, 34, 35, 36, 37] which show that while most water models reproduce the observed decrease in surface tension as temperature increases, they tend to underestimate γ by amounts between 25 and 50 percent. Only Alejandre *et al.*, Huang *et al.*, and Shi *et al.* [31, 37, 38] report adequate agreement with experimental data. However, as we show below, the apparent agreement of both Alejandre *et al.* [31] and Shi *et al.* [37] is the result of inadequate simulation time. Alejandre *et al.* also employ a reciprocal-space mesh that is too coarse, while Huang *et al.* report values only for the SPC and SPC/E models at 298 K [38].

Our primary goal is to study capillary waves at the liquid-vapor interface of water, and to distinguish between various functional representations for the density profile near the interface. Additionally, we first determine the surface tension as a function of temperature for six commonly used three- and four-point models of water, in part to establish a basis for comparison with the capillary-wave simulations.

In Section II, we provide a brief overview of methods for computing the surface tension from molecular simulation data, of the various water models examined in this study, and of the simulation methods employed. Section III presents our findings on the temperature dependence of the surface tension, as well as the effects of the tail correction, interaction cutoffs, and reciprocal-space mesh refinement. We discuss the results obtained from the analysis of capillary waves at the liquid-vapor interface

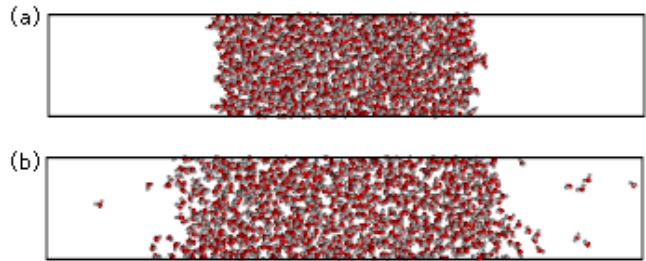


FIG. 1: (Color online) Sample simulation cell, showing equilibrated configurations of 1000 SPC/E water molecules at (a) 300 K and (b) 500 K. The dimensions of the cell are $L_x = L_y = L_{\parallel} = 2.3\text{ nm}$ and $L_z = L_{\perp} = 13.5\text{ nm}$.

in Section IV before offering our conclusions in Section V.

II. MODELS AND METHODOLOGY

A. Surface tension

1. Thermodynamic method

There are two primary methods used to compute the surface tension using molecular simulations. The first approach, developed by Tolman [39] and refined by Kirkwood and Buff [40], computes the surface tension as an integral of the difference between the normal and tangential pressures $p_{\perp}(z)$ and $p_{\parallel}(z)$:

$$\gamma_p = \frac{1}{2} \int_{-\infty}^{\infty} (p_{\perp}(z) - p_{\parallel}(z)) dz, \quad (1)$$

where, in our geometry (see Figure 1),

$$\begin{aligned} p_{\perp}(z) &= p_z(z), \\ p_{\parallel}(z) &= (p_x(z) + p_y(z))/2. \end{aligned}$$

The dominant contributions to the integral in Eq. (1) occur near the interface; in the bulk away from the interface, $p_{\perp} = p_{\parallel}$ and the integrand vanishes. For the specific case shown in Figure 1, where the interface separates a bulk liquid from its corresponding vapor phase, the integral in Eq. (1) can be replaced with an ensemble average of the difference between the normal and tangential pressures,

$$\gamma_p = \frac{L_z}{2} \langle p_{\perp} - p_{\parallel} \rangle = \frac{L_z}{2} \left[\langle p_z \rangle - \frac{\langle p_x \rangle + \langle p_y \rangle}{2} \right]. \quad (2)$$

The outer factor of $1/2$ in Eq. (2) accounts for the presence of two liquid-vapor interfaces.

In most numerical simulations, the interatomic and electrostatic interactions are only applied within a cutoff

TABLE I: Parameters for commonly used three- and four-point models of water

Parameter	SPC/E	TIP3P	TIP3P-C	TIP3P-Ew	TIP4P	TIP4P-Ew
q_H	0.410	0.417	0.417	0.415	0.520	0.5242
q_O	-0.820	-0.834	-0.834	-0.830		
q_M					-1.040	-1.0484
θ_{HOH} , deg	109.47	104.52	104.52	104.52	104.52	104.52
l_{OH} ,	1.0	0.9572	0.9572	0.9572	0.9572	0.9572
l_{OM} ,					0.1500	0.1250
ϵ_{OO} , kcal/mol	0.1553	0.1521	0.1521	0.102	0.1550	0.16275
σ_{OO} ,	3.166	3.1506	3.1507	3.188	3.1536	3.16435
ϵ_{OH} , kcal/mol			0.0836			
σ_{OH} ,			1.7753			
ϵ_{HH} , kcal/mol			0.0460			
σ_{HH} ,			0.4000			

range r_c . The introduction of the cutoff in the interparticle potential reduces the surface tension in much the same way that the introduction of a cutoff reduces the bulk pressure at constant density. Thus, the simulation result γ_p will underestimate the total surface tension; a better estimate of the total surface tension can be obtained from

$$\gamma = \gamma_p + \gamma_{tail}, \quad (3)$$

where γ_{tail} , the tail correction for γ_p , can be determined from [41, 42]

$$\gamma_{tail} = \frac{\pi}{2} \int_{-\infty}^{\infty} \int_{-1}^1 \int_{r_c}^{\infty} r^3 U'(r) g(r) (1 - 3s^2) \times \\ \left(\rho(z) \rho(z - sr) - (\rho_G(z))^2 \right) dr ds dz, \quad (4)$$

where $U(r)$ is the pairwise potential, $g(r)$ is the radial distribution function, $\rho(z)$ is the observed interfacial profile, and $\rho_G(z)$ is a Gibbs dividing surface:

$$\rho_G(z) = \rho_c + \frac{\Delta\rho}{2} \text{sgn}(z). \quad (5)$$

Although the use of the tail correction in Eq. (3) improves the estimate of the surface tension, its use is restricted to systems in which the two phases contain the same components; for composite systems, such as water at the surface of a solid, only γ_p should be used.

We assume in Eqs. (4) and (5) that the liquid-vapor interface is centered at $z = 0$. In Eq. (5), $\rho_c = (\rho_l + \rho_v)/2$ is the average density of the two phases, and $\Delta\rho = \rho_l - \rho_v$ is the difference between the average densities of the two phases. Thus, $\rho_G(z) = \rho_v$ for $z < 0$ and ρ_l for $z > 0$. There are multiple possible choices for determining the observed density profile $\rho(z)$. Although it is possible to use the profile calculated from the simulation directly, both the tail-correction and capillary-wave calculations are simplified by fitting the profile to a function. In the present study, the density profile is fitted to both an error function and a hyperbolic tangent function, as discussed in the following section.

2. Capillary-wave method

The thermodynamic approach for computing surface tension assumes a sharp liquid-vapor interface when in reality it is quite rough. The roughness of the interface increases at high temperatures, as seen in Figure 1. A second method for computing the surface tension assumes that the observed magnitude of the fluctuations is derived from two sources: an intrinsic contribution plus a logarithmic term that represents broadening of the interface as a result of the capillary waves [1, 8, 43, 44, 45, 46].

If the contributions from capillary waves can be decoupled from density fluctuations, then the surface tension can be computed by determining the interfacial profiles for a number of different system sizes. The relationship between the observed interfacial width Δ and the intrinsic interfacial width Δ_0 is given by

$$\Delta^2 = \Delta_0^2 + \frac{k_B T}{2\pi\gamma_w} \ln \left(\frac{L_{\parallel}}{B_0} \right), \quad (6)$$

where $L_{\parallel} = L_x = L_y$ is the length of the interface, and B_0 is a characteristic length scale related to the short-wavelength cutoff in the interfacial behavior. It is unnecessary to determine B_0 before computing the surface tension γ_w .

Computation of γ_w requires the scaled density profile,

$$\Psi(z) = \frac{2}{\rho_L - \rho_V} \left(\rho(z) - \frac{\rho_L + \rho_V}{2} \right), \quad (7)$$

in the z -direction. Given $\Psi(z)$, the variance in the derivative of the profile $f(z) = \Psi'(z)$ can be computed in either real or reciprocal (Fourier) space:

$$\Delta^2 = \frac{\int_{-\infty}^{\infty} z^2 f(z) dz}{\int_{-\infty}^{\infty} f(z) dz} = -\frac{1}{\tilde{f}(0)} \left[\frac{d^2 \tilde{f}(q)}{dq^2} \right]_{q=0}, \quad (8)$$

where $\tilde{f}(q)$ is the Fourier transform of $f(z)$. The simple form of Eq. (8) suggests that fitting the profile $\Psi(z)$ to a functional form will be both more convenient and

lead to more accurate results than using the raw profile data. Several different functional forms for $\Psi(z)$ have been proposed in the literature. Relying on mean-field arguments, most previous theoretical and computational studies of surface tension have fitted the profile to a hyperbolic tangent function [23, 31, 41, 42],

$$\Psi_t(z) = \tanh\left(\frac{2z}{w_t}\right), \quad (9)$$

while Huang and Webb [43] and Beysens and Robert [44] propose the use of an error function,

$$\Psi_e(z) = \operatorname{erf}\left(\frac{\sqrt{\pi}z}{w_e}\right). \quad (10)$$

If the density profile $\Psi(z)$ is fitted to a hyperbolic tangent function Eq. (9), then from Eq. (8) we find that [8]

$$\Delta_t^2 = \pi^2 w_t^2 / 48,$$

while for an error function Eq. (10), the interfacial width Δ_e^2 is given by

$$\Delta_e^2 = w_e^2 / 2\pi.$$

We will show that there is a significant discrepancy between the surface tensions obtained from the hyperbolic tangent profile, Eq. (9), and the error function profile, Eq. (10), with the error function giving results in closer agreement with Eq. (2).

B. Water models

We consider four different three-point models: the SPC/E model; the original TIP3P model; the modification of the TIP3P model [47] implemented in CHARMM (hereafter referred to as TIP3P-C); and the TIP3P-Ew model [11], a recent reparameterization incorporating the effects of Ewald summation. The parameters for the different water models are summarized in Table I.

The basic structure of the different models are similar. The common features of all models include a specified oxygen-hydrogen bond length l_{OH} and hydrogen-oxygen-hydrogen bond angle θ_{HOH} , a charge on each hydrogen atom, and a Lennard-Jones 12-6 potential describing the interaction between the oxygen atoms,

$$U_{LJ}(r_{OO}) = \begin{cases} 4\varepsilon_{OO} \left[\left(\frac{\sigma_{OO}}{r_{OO}} \right)^{12} - \left(\frac{\sigma_{OO}}{r_{OO}} \right)^6 \right], & r_{OO} \leq r_c \\ 0, & r_{OO} > r_c \end{cases}, \quad (11)$$

where ε_{OO} and σ_{OO} are the model-dependent well depth and equilibrium O-O distance, and r_{OO} is the distance between oxygen atoms. The TIP3P-C model incorporates hydrogen-hydrogen and hydrogen-oxygen Lennard-Jones interactions as well.

In addition to the Lennard-Jones interaction, there are electrostatic interactions between the charge sites:

$$U_{es}(r_{ij}) = \sum_{i=1}^N \sum_{j=1}^N \frac{q_i q_j}{4\pi\varepsilon_0 r_{ij}}, \quad (12)$$

where q_α is the charge on atom α , and r_{ij} is the distance between atoms i and j in the simulation box. Previous studies have shown that significant variations in the values obtained for surface tension can occur depending upon how the sum in Eq. (12) is performed [32]. Except in Section III C, Ewald summations were used throughout our simulations.

We also consider a pair of four-point water models: the TIP4P model [17], and the TIP4P-Ew model [12], a recent reparameterization designed to account for the presence of long-range interactions. The four-point models introduce a bare charge at a new site, designated M , located on the bisector of the HOH bond angle; the charge is of strength q_M . The forces acting on the massless site are distributed to the O and H atoms in the same molecule [48]:

$$\begin{aligned} \mathbf{F}_{ij,O} &= (1 - 2a) \mathbf{F}_{ij,M}, \\ \mathbf{F}_{ij,H} &= a \mathbf{F}_{ij,M}, \end{aligned}$$

where $a = l_{OM} / (l_{OH} \cos(\theta_{HOH}/2))$ and $\mathbf{F}_{ij,M}$ is the force acting on the massless site associated with oxygen i due to atom j [49]¹. For the TIP4P model, the charge is located $l_{OM} = 0.15 \text{ \AA}$ away from the oxygen atom. The TIP4P-Ew model changes the values of l_{OM} , the charge q_M , as well as the separation σ_{OO} and well-depth ε_{OO} of the Lennard-Jones interaction.

C. Simulation method

1. Thermodynamic method

To determine the surface tension of the various three-point water models, 1000 molecules were placed into a periodic, rectangular box of dimensions $L_x = L_y = L_{\parallel} = 2.3 \text{ nm}$ and $L_z = L_{\perp} = 13.5 \text{ nm}$. The increased system size in the z -direction minimizes the interactions of water molecules in the liquid phase with their z -periodic images through the long-range Coulombic interactions in Eq. (12). Similarly, 1000 molecules of the four-point models were simulated in a box with dimensions $L_x = L_y = L_{\parallel} = 2.7 \text{ nm}$ and $L_z = L_{\perp} = 12.0 \text{ nm}$, each also containing 1000 molecules. The initial configuration was constructed by placing the water molecules

¹ In the case of four-point water models, while the contribution to the virial from the Lennard-Jones interactions can be computed using the more computationally efficient form $\sum_i \mathbf{r}_i \cdot \mathbf{f}_i$, the contribution to the virial from short-range electrostatic forces is computed using the pairwise form $\sum_{i>j} \mathbf{r}_{ij} \cdot \mathbf{f}_{ij}$.

at the center of a simple cubic lattice with 7 molecules each in the x - and y -directions, and the z -spacing chosen to create a density of 0.98 g cm^{-3} for the three-point models, and 1.00 g cm^{-3} for the four-point models. The same starting configuration was used for all simulations of a given water model. At equilibrium, the thickness of the slab in the z -direction varied between approximately 5.5 nm at 300 K and 7.5 nm at 500 K.

For each of the six models examined, molecular dynamics (MD) simulations were performed in the NVT ensemble in 25-degree increments between 300 K and 500 K using the LAMMPS simulation package [50]. The cutoff for the Lennard-Jones potentials and the short-range cutoff for the electrostatic potentials were set to 10 Å, unless otherwise specified. The bond lengths and bond angles of the various models were constrained using the SHAKE technique [51]. The equations of motion were integrated using the Verlet algorithm with velocity rescaling to control the temperature. The difference in the surface tension between simulations performed with velocity rescaling and those with a Nosé-Hoover thermostat with a damping constant of 100 ps^{-1} was significantly less than the simulation uncertainty. Each simulation was performed for a total of 2 ns with time step $\Delta t = 1 \text{ fs}$. The system was allowed to equilibrate for 1 ns; data from the second 1 ns were used to compute the surface tension.

The electrostatic interactions were calculated using the particle-particle particle-mesh (PPPM) technique of Hockney and Eastwood [52]. The mesh spacing in this work was selected to ensure that the root-mean-squared accuracy of the force calculation was within 10^{-4} ; the resulting grid was of dimensions $12 \times 12 \times 48$. Most previous simulations were carried out with a maximum of $h_z^{\text{max}} = 20$ cells in the z -direction [31, 32]. In several of those studies, simulations were carried out with $h_z^{\text{max}} = 10$ or less, and some did not include long-range electrostatic interactions at all [33]. We consider the effects of mesh refinement on the surface tension in Section III D.

2. Capillary-wave method

Observation of capillary waves requires simulations with larger interfacial surface areas than were used in the thermodynamic method above. Consequently, we studied systems with $L_x = L_y = L_{\parallel}$ varying between 9.2 nm and 46.0 nm. The resulting simulations used to compute the surface tension have surface areas between 84.6 nm^2 and 2116.0 nm^2 , and contained between 16,000 and 400,000 water molecules. To construct the initial configuration, we take an equilibrated sample and replicate it multiple times in the x - and y -directions. The SPC/E model was used for this study, as it was the most computationally efficient of the models studied.

To ensure that artifacts from the replication process were eliminated, the simulation time varied between 1.0 ns and 6.0 ns as an increasing function of L_{\parallel} . Only the

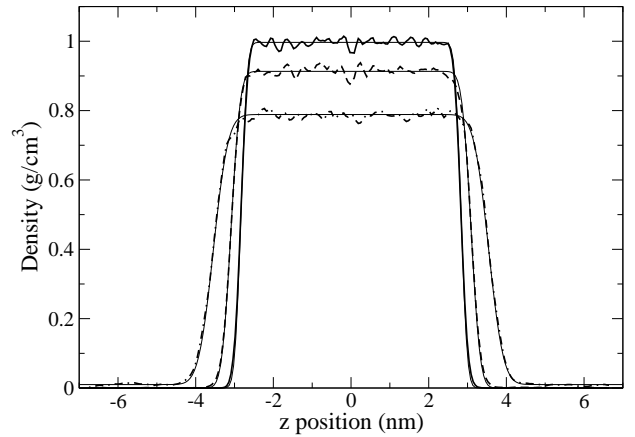


FIG. 2: Density profiles for the SPC/E model of water at 300 K (thick solid line), 400 K (thick dashed line), and 500 K (thick dashed-dotted line). Fits to error functions are shown as thin solid lines.

last 750 ps of the simulation were used for recording data; the preceding steps were used for equilibration and discarded. We output the position of every atom after every 5000 timesteps, and then assigned each atom to one of 500 bins depending on its location in the z -direction. To ensure that the interfacial profile was not altered by drifts in the density profile, the profile was shifted so that the center of the mass was located at $z = 0$. Sample profiles for the SPC/E model of water at several temperatures are shown in Figure 2. After the average density profile $\rho(z)$ was computed, the two halves of the profile, on either side of $z = 0$, were averaged together, rescaled to values between -1 and 1 using Eq. (7), and then fitted to hyperbolic tangent and error functions of the form of Eq. (9) and Eq. (10).

III. THERMODYNAMIC SURFACE TENSION: RESULTS AND DISCUSSION

A. Temperature dependence

The surface tension $\gamma = \gamma_p + \gamma_{\text{tail}}$ of the various water models, computed using Eq. (2), are collected in Table II. Results for the three-point models are shown in Figure 3(a) as a function of temperature. Using the method of Flyvbjerg and Petersen [53], the uncertainty in the results was found to be between 2.4 and 3.0 mN/m. Comparing the four three-point models, we find that SPC/E model is the closest to the experimental data, with better agreement at higher temperatures. For most temperatures, the various TIP3P models agree with the SPC/E model within the uncertainty of the simulation. Although the three-point models considered do not achieve agreement with experimental data, the overall temperature dependence of γ for the models is in good agreement with the experimental data. For the three-point mod-

TABLE II: Surface tension^a for three- and four-point water models, including tail correction

Temperature (K)	Surface Tension, γ (mN/m)						Expt. ^b
	SPC/E	TIP3P	TIP3P-Ew	TIP3P-C	TIP4P	TIP4P-Ew	
300	55.4	51.1	47.4	48.8	53.6	61.2	71.7
325	47.9	45.9	43.6	47.5	50.9	55.6	67.6
350	47.0	42.8	39.2	45.7	45.7	52.7	63.2
375	44.6	37.8	37.7	39.9	41.4	48.1	58.4
400	37.6	35.5	34.3	36.9	35.9	43.5	53.3
425	32.0	31.5	28.9	31.9	31.2	38.6	47.9
450	30.6	27.3	25.9	28.2	25.7	34.5	42.1
475	26.8	24.7	23.2	23.2	19.1	29.3	36.0
500	23.2	17.0	16.9	18.1	15.2	24.8	29.5

Notes: ^aUncertainty for all simulation results is between 2.4 and 3.0 mN/m. ^bExperimental data taken from Refs. [26, 27, 28]; data above 400 K is extrapolated from quadratic fit provided in Ref. [27].

TABLE III: Interfacial properties of SPC/E water as a function of temperature, for $r_c = 10$ and $L_{\parallel} = 2.3$ nm

Temperature T , K	Interface thickness w_e	Liquid density ρ_L , g/cm ³	Vapor density ρ_V , g/cm ³	Tail correction γ_{tail} , mN/m
300	3.12	0.990	0.0005	5.5
325	3.37	0.977	0.0008	5.2
350	3.75	0.959	0.0005	5.0
375	4.22	0.941	0.0005	4.8
400	4.63	0.913	0.0015	4.5
425	5.23	0.886	0.0023	4.1
450	5.74	0.855	0.0049	3.8
475	6.00	0.818	0.0093	3.5
500	7.54	0.779	0.0199	3.0

els, γ is generally between 15 mN/m and 20 mN/m less than the experimental data, especially in the temperature range $300 \text{ K} < T < 425 \text{ K}$.

Alejandre *et al.* [31] and Shi *et al.* [37] reported excellent agreement with experimental results for the SPC/E model. However, our results for the SPC/E model clearly disagree with their data as well as with experimental results, although the simulations were performed under essentially identical conditions with respect to the number of molecules and the dimensions of the system, potentials employed, temperature range, and cutoffs. We study the potential causes of the disagreement in the results below in Sections III C and III D.

Results for the four-point models as a function of temperature are shown in Figure 3(b). The uncertainty for

the four-point models is the same as for the three-point models. Like the three-point models, the four-point models underestimate the surface tension, with the TIP4P model offering results comparable to the TIP3P-C and TIP3P-Ew models, while the performance of the TIP4P-Ew model is significantly closer to the experimental data than any of the other models examined here. Unlike the TIP3P models, at most temperatures considered here, the TIP4P and TIP4P-Ew models do not agree within simulation uncertainty.

TABLE IV: Surface tensions γ_p and γ and liquid-phase density ρ_L for the SPC/E model as a function of LJ cutoff r_c , with and without tail correction, at 300 K

r_c (Å)	γ_p (mN/m)	γ (mN/m)	ρ_L (g/cm ³)
10.0	46.3	51.8	0.990
12.0	51.2	55.0	0.992
14.0	47.9	50.6	0.994
16.0	49.7	51.8	0.996
18.0	49.9	51.5	0.996
20.0	52.8	54.1	0.995

TABLE V: Surface tension γ_p and γ for the SPC/E model as a function of LJ cutoff

T (K)	γ_p (mN/m)		γ (mN/m)	
	$r_c = 10$	$r_c = 16$	$r_c = 10$	$r_c = 16$
300	49.9	50.2	55.4	52.3
325	42.8	48.7	47.8	50.7
350	42.2	47.2	47.0	49.1
375	40.0	40.3	44.6	42.1
400	33.3	37.7	37.6	39.4
425	28.1	33.5	32.0	35.0
450	27.0	29.2	30.6	30.6
475	23.6	23.6	26.8	24.9
500	20.5	22.3	23.2	23.3

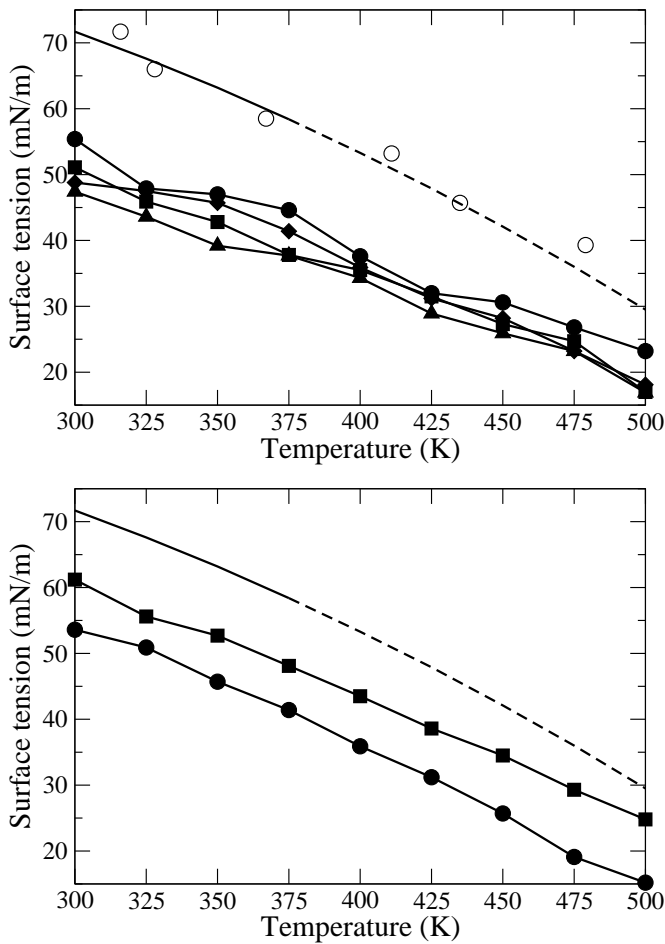


FIG. 3: (Top figure) Surface tension of the three-point models of water as a function of temperature: SPC/E (filled circles), TIP3P (squares), TIP3P-C (triangles), and TIP3P-Ew (diamonds). Simulation data from Alejandre *et al.* [31] (open circles) are included for comparison. (Bottom figure) Surface tension of the four-point models of water as a function of temperature: TIP4P (circles) and TIP4P-Ew (squares). In both figures, experimental data [26, 27, 28] (solid curve) and extrapolation of quadratic fit to higher temperatures (dashed curve) are included for comparison.

B. Tail correction

While tail corrections can exist for both the Lennard-Jones and the electrostatic interactions, by using Ewald summations, we avoid the need for a Coulombic tail correction. In evaluating the tail correction, Eq. (4) for the Lennard-Jones potential in the region $r \gg \sigma$, $dU(r)/dr \approx 24\epsilon\sigma^6 r^{-7}$. Assuming that for $r > r_c$, the radial distribution function $g(r) \approx 1$ and that the density profile is an error function of the form Eq. (10), we

can evaluate Eq. (4). After integration over s ,

$$\frac{\gamma_{tail}}{12\pi\epsilon\sigma^6} = \int_{-\infty}^{\infty} \int_{r_c}^{\infty} \frac{\text{erf}(\xi z)}{\sqrt{\pi}\xi^3 r^7} e^{-\xi^2(r+z)^2} \times \\ \left(\xi^2 z(r-z) + e^{4\xi^2 r z} (\xi^2 z(z+r) + 1) - 1 \right) \\ - \frac{z \text{erf}(\xi z)}{2\xi^2 r^7} (3 - \xi^2(z^2 - r^2)) f(\xi, r, z) dr dz, \quad (13)$$

where $\xi \equiv \sqrt{\pi}/w_e$ and

$$f(\xi, r, z) = \text{erf}(\xi(r+z)) + \text{erf}(\xi(r-z)).$$

Eq. (13) is then evaluated numerically for each density profile. For the SPC/E model of water, the interfacial thickness, density difference, and tail correction are shown in Table III. Because of the existence of capillary waves at the interface, as shown in Section IV, the interfacial thickness parameter w_e depends logarithmically on the length L_{\parallel} of the interfacial surface.

The tail correction depends strongly upon the Lennard-Jones parameters, scaling as $\epsilon\sigma^6$, and decays exponentially as a function of the chosen interaction cutoff r_c . Because ϵ_{OO} and σ_{OO} are approximately equal for the SPC/E and TIP3P models, the tail corrections at all temperatures are almost identical for the two models. While the TIP3P-C has additional tail corrections for the O-H and H-H interactions, their magnitudes are negligible in comparison to the correction for the O-O interaction. Only the TIP3P-Ew model, which has a significantly smaller value for the Lennard-Jones interaction strength ϵ_{OO} , has a noticeably different tail correction from the other three-point models. The tail corrections for the four-point models are likewise close to that of the SPC/E model, with the TIP4P model having a slightly smaller tail correction and the TIP4P-Ew model a slightly larger tail correction.

C. Cutoff effects

The original parameterizations for the SPC/E and TIP3P models of water employed cutoffs for both electrostatic and Lennard-Jones interactions [16, 17]. To study the effect of varying the electrostatic cutoff, we applied a short-range cutoff to both the LJ and electrostatic potentials of the SPC/E model, truncating the potentials at $r_{cut} = 10, 12, 14, 16, 18,$ and 20 \AA . Using Eq. (2) to determine the surface tension, we found that the estimated values of the surface tension were nonsensical, ranging between -3700 and 1700 mN m^{-1} , with no value smaller in magnitude than 140 mN m^{-1} . This shows that truncated electrostatic potentials are inappropriate for use in the determination of the surface tension of water.

To determine the effect of varying only the range of the Lennard-Jones interaction on γ_p before incorporating the tail correction, we performed runs for the SPC/E model at 300 K with LJ cutoffs of 10, 12, 14, 16, 18, and 20 \AA ,

using the PPPM Ewald technique for the electrostatic forces. The starting configuration for these runs was the final configuration from the 300 K simulation used to compute the surface tension in Section III A. The resulting values of the surface tension are shown in Table IV. The values for the surface tension are within the simulation uncertainties, although they tend to rise with increasing r_c . This is further reflected in the density profiles, which show that the liquid-phase density ρ_L increases with r_c for values of r_c between 10 Å and 18 Å. The overall effect of the choice of r_c can be seen when comparing the surface tensions of SPC/E water in the temperature range 300 K to 500 K for LJ cutoffs of 10 Å and 16 Å. The resulting data are shown in Table V. The data demonstrate that the surface tensions for 10 Å and 16 Å cutoffs are equal, within simulation uncertainty, after the corresponding tail corrections have been applied to each set of data. Thus, the 10 Å Lennard-Jones cutoff with long-range tail corrections is sufficiently accurate for computing the surface tension.

D. Reciprocal space accuracy dependence

Alejandre *et al.* [31] found that the surface tension depended on the mesh refinement $|\mathbf{h}^{\max}|$ used to evaluate the long-range Coulombic interactions. To test the dependence of γ_p on $|\mathbf{h}^{\max}|$, we show results in Figure 4 for three different models as a function of $|\mathbf{h}^{\max}|$. From the figure, several trends become apparent. First, for both the TIP3P and TIP3P-Ew models, the long-time average of the surface tension depends significantly on the value $|\mathbf{h}^{\max}|$: the long-time average for a $5 \times 5 \times 20$ mesh ($|\mathbf{h}^{\max}| = 20$, rms accuracy 4.0×10^{-3}) is between 15 and 20 mN m^{-1} larger than for a $12 \times 12 \times 48$ mesh ($|\mathbf{h}^{\max}| = 50$, rms accuracy 10^{-4}). For larger values of $|\mathbf{h}^{\max}|$, there is no significant adjustment in the surface tension. Additionally, as found above, for a given value of the precision, there is little difference in the long-time average of the two models.

For the SPC/E model, there is little difference between the equilibrium values for the $5 \times 5 \times 20$ mesh and the $12 \times 12 \times 48$ mesh. However, it takes approximately 1 ns to achieve agreement between the two precision levels; before this, the less-refined mesh has a significantly greater surface tension. In the work of Alejandre *et al.*, the total simulation time was only 0.375 ns. After 0.375 ns, the average surface tension from our simulation using the $5 \times 5 \times 20$ mesh was approximately $\gamma = 60 \text{ mN m}^{-1}$, which closely corresponds with the result $\gamma = 60.6 \text{ mN m}^{-1}$ obtained in the earlier study. However, for long simulation times, the surface tension of the SPC/E model does not exhibit a strong dependence on the mesh size. Consequently, since the long-time averages are essentially equal within simulation uncertainty, we have used the finer $12 \times 12 \times 48$ mesh refinement for all of the simulations reported in this paper unless otherwise specified.

To further demonstrate that the accuracy of the

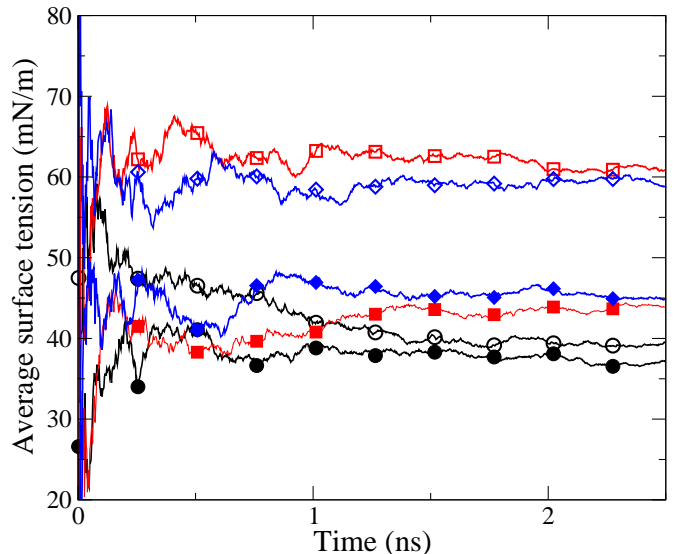


FIG. 4: (Color online) Equilibration of the surface tension of the SPC/E (black circles), TIP3P (red squares), and TIP3P-Ew (blue diamonds) models of water for rms \mathbf{k} -space accuracies of 4×10^{-3} (dashed curves, open symbols) and 10^{-4} (solid curves, solid symbols).

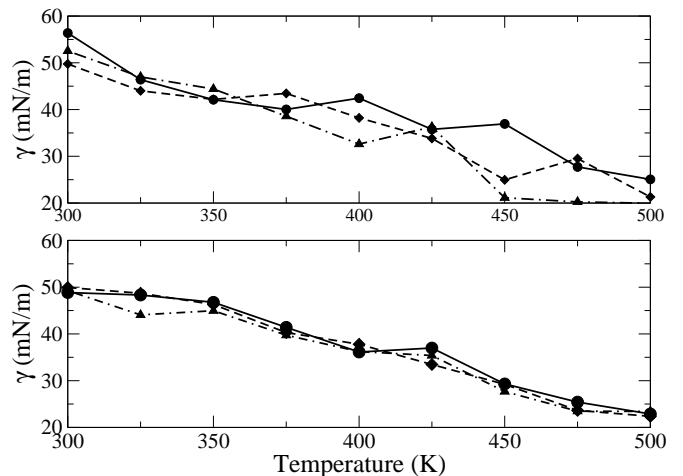


FIG. 5: Surface tension for the SPC/E model of water as a function of mesh accuracy averaged over (top) 125-375 ps and (bottom) 1-2 ns for a $5 \times 5 \times 20$ mesh (circles), a $12 \times 12 \times 48$ mesh (diamonds), and a $20 \times 20 \times 80$ mesh (triangles).

reciprocal-space calculation does not affect the results for the surface tension of the SPC/E model when averaged over sufficiently long times, we performed simulations of the SPC/E model, as described above, with \mathbf{k} -space meshes of $5 \times 5 \times 20$, $12 \times 12 \times 48$, and $20 \times 20 \times 80$, corresponding to rms accuracies of 4×10^{-3} , 10^{-4} , and 10^{-5} , respectively. The results are shown in Figure 5 for the time ranges of 125 to 375 ps, used by Alejandre *et al.*, and 1 to 2 ns, used in the present work. Clearly, the

TABLE VI: Comparison of surface tension for the SPC/E model as a function of calculation method

T (K)	Surface tension, mN/m		
	Capillary-wave		Pressure-integration, γ_p
	Erf, γ_w	Tanh, γ_w	
300	46.1	36.5	49.9
400	32.0	27.8	33.1
500	19.0	19.0	20.2

TABLE VII: Surface tension for the SPC/E model as a function of system size at 300 K

Interfacial length L_{\parallel} , Å	γ_p (mN/m)	γ (mN/m)
2.3	49.9	55.4
9.2	52.0	57.5
11.5	51.5	57.0
13.8	51.8	57.3
16.1	51.9	57.4
23.0	51.6	57.1
34.5	52.0	57.5
46.0	51.8	57.3

results for the shorter time range (125 to 375 ps) have not converged: there is significant disagreement of as much as 20 mN/m, particularly at higher temperatures. However, for longer times, the results have converged, with the differences among the three mesh refinements being essentially within simulation uncertainty. It is interesting to note that the converged surface tensions of the different mesh refinements corresponds very closely to the profile obtained for the intermediate mesh refinement ($12 \times 12 \times 48$) after 375 ps. Our intermediate mesh refinement is comparable to the most refined \mathbf{k} -space mesh considered by Alejandre *et al.* [31] (shown in Fig. 7 of their paper for a single, instantaneous configuration).

IV. CAPILLARY WAVES

The interfacial width Δ^2 was computed for various system sizes as described in Section II. The resulting plots of Δ^2 versus $\ln L$ were computed and the value of γ_w extracted using Eq. (6). A plot showing the data obtained for 300 K for the SPC/E water model is shown in Figure 6; the resulting values of γ_w for the two functional forms at 300 K, 400 K, and 500 K are shown in Table VI.

Our results indicate that at all three temperatures, good agreement between the pressure-integration estimate of the surface tension, γ_p , and the capillary-wave estimate of the surface tension, γ_w , is obtained only if the interfacial density profile is fit to an error function. There is substantial disagreement between the error function and hyperbolic tangent functions at lower temperatures: the hyperbolic tangent profile always yields lower estimates than the error function profile. However, the

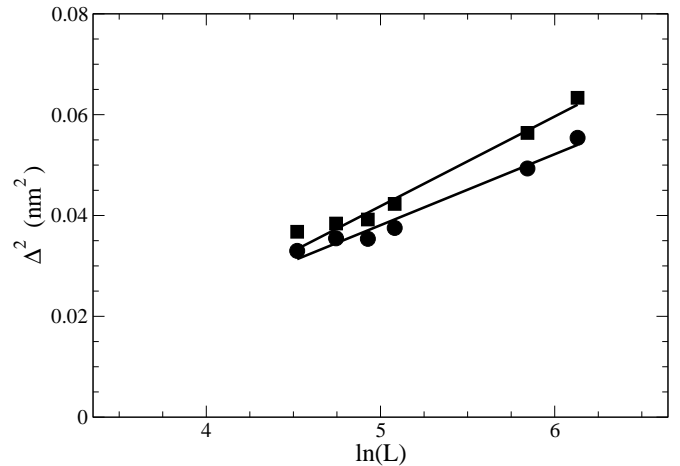


FIG. 6: Regression fit of Eq. (6) for hyperbolic tangent (diamonds) and error function (circles) profiles at 300 K.

magnitude of the discrepancy between the two estimates of γ decreases the two narrows as temperature increases, and essentially vanishes at 500 K.

In addition to computing the surface tension γ_w , we can also compute an upper-bound estimate for the intrinsic interfacial width Δ_0 [8]. After obtaining the slope α_w and intercept β_w for the least-squares fit of Eq. (6), we assume that the parameter $B_0 = c\Delta_0$, where c is a constant to be specified. The intercept β_w and Δ_0 are then related by

$$\beta_w = \Delta_0^2 - \alpha_w \ln(c\Delta_0). \quad (14)$$

For values of c less than some threshold c^* , there is no real solution to (14); above the threshold, Δ_0 quickly decays as c increases. Thus, Δ_0 has a maximum at the threshold value $c = c^*$ where the imaginary part of the solution vanishes. For the system sizes under consideration, we find that the maximum intrinsic width $\Delta_0 \approx 0.8 \text{ \AA}$, 1.0 \AA , and 1.5 \AA at $T = 300 \text{ K}$, 400 K , and 500 K .

Further evidence that fitting the density profile to an error function yields more accurate results than fitting to a hyperbolic tangent function can be seen by comparing the density fits themselves. As shown in Figure 7, although the two profiles are similar, the error function fit more closely adheres to simulation results than the hyperbolic tangent profile. Although the χ^2 parameter for both functional fits was relatively small, the coefficient for the hyperbolic tangent χ^2 parameter ($\sim 10^{-3}$) was approximately two orders of magnitude larger than the corresponding error function χ^2 parameter ($\sim 10^{-5}$). The greater accuracy of the error function is further seen by comparing the magnitude of the differences between the simulation results and the fitted functional profiles, as shown in Figure 8.

In addition to observing capillary wave behavior, the larger simulations can be used to study the effect of the interfacial area L_{\parallel}^2 on the surface tension computed using

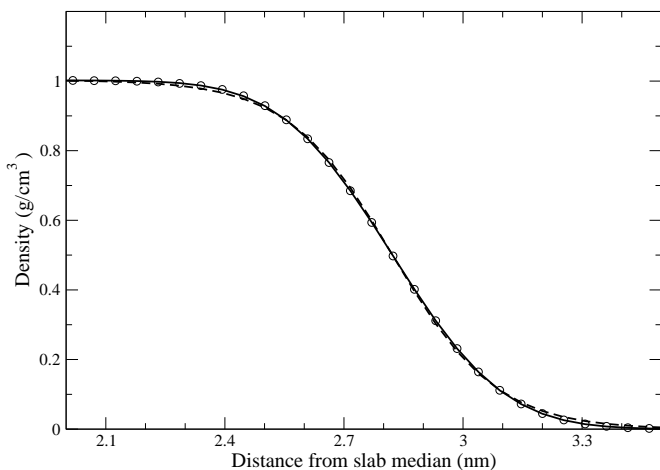


FIG. 7: Density profile in the interfacial region for a slab of 400,000 SPC/E water molecules at 300 K ($L_{\parallel} = 46.0$ nm). Simulation results are shown as circles; fits to error function (solid curve) and hyperbolic tangent function (dashed curve)

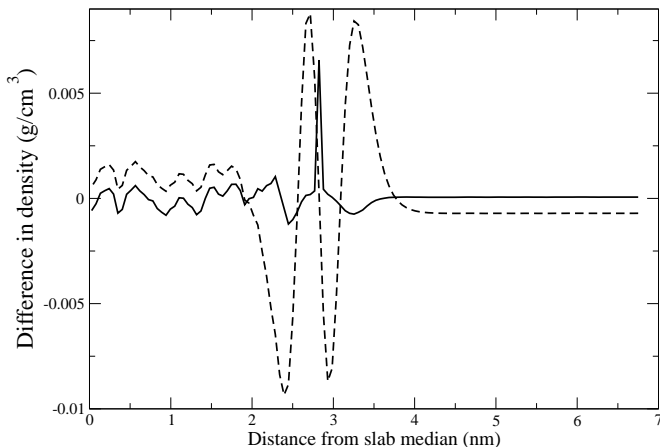


FIG. 8: Difference between simulation results and the error function (solid curve) and the hyperbolic tangent (dashed curve) fits for the same system shown in Figure 7.

Eqs. (2) and (13). Since surface tension is an intensive property, it should be independent of L_{\parallel}^2 . Although Eq. (13) is a slowly decreasing function of the parameter w_e , over the range of values for w_e and Δ^2 considered here, the tail contribution γ_{tail} varies by less than 2%. Thus,

we expect the simulation values for the surface tension to remain constant, independent of L_{\parallel} . Examining the results for the surface tension γ_p (without tail correction) versus the system size N , as shown in Table VII, we find a slight increase in γ as L_{\parallel} increases, although the results remain within simulation uncertainty, even for large values of L_{\parallel} .

V. CONCLUSIONS

An investigation of surface tension as a function of temperature for a number of popular three- and four-point water models shows systematic disagreement between experimental and simulation results for all six models considered. All six models considered consistently underestimate the surface tension relative to the experimental data. The TIP4P-Ew model is closest to the experimental data, although not in quantitative agreement.

Examining the SPC/E model in greater detail, we have illustrated the importance of having a sufficiently long simulation time and sufficiently fine \mathbf{k} -space mesh: significant variations in the surface tension can result if the equilibration period is too short. In the SPC/E, TIP3P, and TIP3P-Ew models, significant variations were also observed if a small number of \mathbf{k} -space vectors are used.

The present study also includes the first in-depth study of the effect of large system sizes on interfacial properties, studying capillary waves for systems of up to 4×10^5 molecules. We have demonstrated that examining capillary waves at the liquid-vapor interface can be used to determine the surface tension of real fluids, and that the use of an error function profile offers better results in comparison to experimental data than the use of a hyperbolic tangent profile. Finally, we note that the interfacial width Δ depends on the interfacial length L_{\parallel} , and that attempting to extract an interfacial width without taking into account the effect of capillary waves [23] is incorrect.

Acknowledgments

The authors would like to thank Steve Plimpton, Paul Crozier, and Amalie Frischknecht for helpful discussions in implementing the TIP4P model. Sandia is a multi-program laboratory operated by Sandia Corporation, a Lockheed Martin Company, for the United States Department of Energy under Contract No. DE-AC04-94AL85000.

[1] F. P. Buff, R. A. Lovett, and F. H. Stillinger, *Phys. Rev. Lett.*, **15**, 621–623 (1965).
 [2] J. Rowlinson and B. Widom, *Molecular Theory of Capillarity*, Clarendon Press, Oxford, 1982.
 [3] K. R. Mecke and S. Dietrich, *Phys. Rev. E*, **59**, 6766–6784 (1999).

[4] S. Senapati and M. L. Berkowitz, *Phys. Rev. Lett.*, **87**, 176101 (2001).
 [5] J. L. Rivera, C. McCabe, and P. T. Cummings, *Phys. Rev. E*, **67**, 011603 (2003).
 [6] M. Nijmeijer, A. Bakker, C. Bruin, and J. Sikkenk, *J. Chem. Phys.*, **89**, 3789 (1988).

- [7] P. Adams and J. Henderson, *Mol. Phys.*, **73**, 1383 (1991).
- [8] M.-D. Lacasse, G. S. Grest, and A. J. Levine, *Phys. Rev. Lett.*, **80**, 309–312 (1998).
- [9] B. Guillot, *J. Molec. Liq.*, **101**, 219–260 (2002).
- [10] J. L. Rivera, M. Predota, A. A. Chialvo, and P. T. Cummings, *Chem. Phys. Lett.*, **357**, 189–194 (2002).
- [11] D. J. Price and C. L. Brooks III, *J. Chem. Phys.*, **121**, 10096–11003 (2004).
- [12] H. W. Horn, W. C. Swope, J. W. Pitera, J. D. Madera, T. J. Dick, G. L. Hura, and T. Head-Gordon, *J. Chem. Phys.*, **120**, 9665–9678 (2004).
- [13] W. L. Jorgensen and J. Tirado-Rives, *Proc. Natl. Acad. Sci.*, **102**, 6665–6670 (2005).
- [14] H. J. C. Berendsen, J. P. M. Postma, W. F. Van Gunsteren, and J. Hermans In *Intermolecular Forces*, B. Pullman, Ed.; Reidel, Dordrecht, 1981; page 331.
- [15] H. A. Stern, F. Rittner, B. J. Berne, and R. A. Friesner, *J. Chem. Phys.*, **115**, 2237–2251 (2001).
- [16] H. J. C. Berendsen, J. R. Grigera, and T. P. Straatsma, *J. Phys. Chem.*, **91**, 6269–6271 (1987).
- [17] W. L. Jorgensen, J. Chandrasekhar, J. D. Madura, R. W. Impey, and M. L. Klein, *J. Chem. Phys.*, **79**, 926–935 (1983).
- [18] K. Watanabe and M. L. Klein, *Chem. Phys.*, **131**, 157–167 (1989).
- [19] M. W. Mahoney and W. L. Jorgensen, *J. Chem. Phys.*, **112**, 8910–8922 (2000).
- [20] J. D. Bernal and R. H. Fowler, *J. Chem. Phys.*, **1**, 515 (1933).
- [21] F. H. Stillinger and A. Rahman, *J. Chem. Phys.*, **60**, 1545–1557 (1974).
- [22] S. W. Rick, S. J. Stuart, and B. J. Berne, *J. Chem. Phys.*, **101**, 6141–6156 (1994).
- [23] I.-F. W. Kuo, C. J. Mundy, B. L. Eggimann, M. J. McGrath, J. I. Siepmann, B. Chen, J. Vieceli, and D. J. Tobias, *J. Phys. Chem. B*, **110**, 3738–3746 (2006).
- [24] P. Mark and L. Nilsson, *J. Phys. Chem. A*, **105**, 9954–9960 (2001).
- [25] P. Mark and L. Nilsson, *J. Comp. Chem.*, **23**, 1211–1219 (2002).
- [26] G. J. Gittens, *J. Coll. Interf. Sci.*, **30**, 406–412 (1969).
- [27] R. Cini, G. Loglio, and A. Ficaldi, *J. Coll. Interf. Sci.*, **41**, 287–298 (1972).
- [28] J. J. Jasper, *J. Phys. Chem. Ref. Data*, **1**, 841 (1972).
- [29] K. Johansson and J. C. Eriksson, *J. Coll. Interf. Sci.*, **40**, 398–405 (1972).
- [30] D. K. Thakur and K. Hickman, *J. Coll. Interf. Sci.*, **50**, 525–531 (1975).
- [31] J. Alejandre, D. J. Tildesley, and G. A. Chapela, *J. Chem. Phys.*, **102**, 4574–4583 (1995).
- [32] S. E. Feller, R. W. Pastor, A. Rojnuckarin, S. Bogusz, and B. R. Brooks, *J. Chem. Phys.*, **100**, 17011–17020 (1996).
- [33] R. S. Taylor, L. X. Dang, and B. C. Garrett, *J. Phys. Chem.*, **100**, 11720–11725 (1996).
- [34] L. X. Dang and T.-M. Chang, *J. Chem. Phys.*, **106**, 8149–8159 (1997).
- [35] V. V. Zakharov, E. N. Brodskaya, and A. Laaksonen, *J. Chem. Phys.*, **107**, 10675–10683 (1997).
- [36] V. V. Zakharov, E. N. Brodskaya, and A. Laaksonen, *Mol. Phys.*, **95**, 203–209 (1998).
- [37] B. Shi, S. Sinha, and V. K. Dhir, *J. Chem. Phys.*, page In press.
- [38] D. M. Huang, P. L. Geissler, and D. Chandler, *J. Phys. Chem. B*, **105**, 6704–6709 (2001).
- [39] R. C. Tolman, *J. Chem. Phys.*, **16**, 758–774 (1948).
- [40] J. G. Kirkwood and F. P. Buff, *J. Chem. Phys.*, **17**, 338–343 (1949).
- [41] G. A. Chapela, G. Saville, S. M. Thompson, and J. S. Rowlinson, *J. Chem. Soc. Farad. Trans.*, **73**, 1133–1144 (1977).
- [42] E. M. Blokhuis, D. Bedeaux, C. D. Holcomb, and J. A. Zollweg, *Mol. Phys.*, **85**, 665–669 (1995).
- [43] J. S. Huang and W. W. Webb, *J. Chem. Phys.*, **50**, 3677–3693 (1969).
- [44] D. Beysens and M. Robert, *J. Chem. Phys.*, **87**, 3056–3061 (1987).
- [45] A. N. Semenov, *Macromolecules*, **27**, 2732–2735 (1994).
- [46] S. W. Sides, G. S. Grest, and M.-D. Lacasse, *Phys. Rev. E*, **60**, 6708–6713 (1999).
- [47] S. R. Durell, B. R. Brooks, and A. Ben-Naim, *J. Phys. Chem.*, **98**, 2198–2202 (1994).
- [48] K. A. Feenstra, B. Hess, and H. J. C. Berendsen, *J. Comp. Chem.*, **20**, 786–798 (1999).
- [49] D. Van der Spoel, E. Lindahl, B. Hess, A. R. Bureun, E. Apol, P. J. Meulenhoff, D. P. Tieleman, A. L. T. M. Sijbers, K. A. Feenstra, R. Van Drunen, and H. J. C. Berendsen, *Gromacs User Manual Version 3.3*, www.gromacs.org, 2005.
- [50] S. J. Plimpton, *J. Comp. Phys.*, **117**, 1–9 (1995).
- [51] J.-P. Ryckaert, G. Ciccotti, and H. J. C. Berendsen, *J. Comp. Phys.*, **23**, 327 (1977).
- [52] R. W. Hockney and J. W. Eastwood, *Computer Simulation Using Particles*, Adam Hilger-IOP Publishing, Bristol, 1988.
- [53] H. Flyvbjerg and H. G. Petersen, *J. Chem. Phys.*, **91**, 461–466 (1989).